

Synchrotron-based Photonuclear Neutron Source for Energy, Medicine and Radiation Testing

Antonio Cammi *,^{a,b,c,d}, Lorenzo Loi ^{a,b}, Andrea Missaglia ^a, David Alesini ^e, Hans Heinrich Braun ^f

^a*Politecnico di Milano, Department of Energy, Via La Masa 34, Milano 20133, Italy*

^b*INFN, Sezione di Milano Bicocca, 20126 Milan, Italy*

^c*Department of Mechanical and Nuclear Engineering, Khalifa University, Abu Dhabi, 127788, United Arab Emirates*

^d*Emirates Nuclear Technology Centre (ENTC), Khalifa University of Science and Technology, Abu Dhabi, 127788, United Arab Emirates*

^e*INFN–Laboratori Nazionali di Frascati, Via E. Fermi 54, Frascati (Roma) 00044, Italy*

^f*Paul Scherrer Institut, Forschungsstrasse 111 5232 Villigen PSI, Switzerland*

Abstract

The global availability of high-intensity neutron sources is restricted by the prohibitive costs of spallation facilities and the decommissioning of aging research reactors, while compact accelerator-driven sources (CANS) are fundamentally limited by target power density and thermal-mechanical stress. Here, we introduce SYNERGY (SYnchrotron-driven NEutron source for Research, energy Generation and therapY), a paradigm-shifting architecture that overcomes these bottlenecks by decoupling charged-particle acceleration from neutron production. By utilizing a storage ring to drive external photoneutron targets via synchrotron radiation, this topological separation ensures targets interact exclusively with a continuous-wave (CW) photon beam, minimizing thermo-mechanical shocks and enabling beam powers exceeding 200 kW per beamline. Through a systematic parametric analysis cross-validated using OpenMC, MCNPX, and FLUKA, we demonstrate single-beamline neutron production rates from 2.8×10^{14} to 1.3×10^{15} n/s. With an inherent multi-beamline capacity feeding up to 50 independent stations, the total facility intensity exceeds 6.0×10^{16} n/s. By bridging the gap between laboratory and national-scale infrastructure, SYNERGY provides a high-intensity, multi-user platform for subcritical systems, medical isotope production, and boron neutron capture therapy.

Keywords: Synchrotron Radiation, Photoneutron Source, CANS, Neutron Production, SYNERGY

1. Introduction

Historically, neutron beam availability has been polarized between two technological extremes [1]. On one end, there are large-scale facilities, namely fission reactors (e.g.,

*Corresponding author. Email address: antonio.cammi@polimi.it

ILL) and spallation sources (e.g., SNS and J-PARC), that provide very high neutron source rates, exceeding 10^{17} n/s. However, these installations require substantial capital investment, complex infrastructure, and centralized operation, which severely limits the accessibility from the user side. In addition, the progressive shutdown of nuclear power plants further constrains the long-term availability of reactor-based neutron sources [2]. On the other end, there are isotopic sources (e.g., ^{252}Cf or Am-Be) that offer simplicity and portability, but with neutron intensities typically below 10^9 n/s [3], which is insufficient for most scientific and industrial applications.

At the same time, the framework of neutron applications has continued to broaden, as comprehensively reviewed by Kiyanagi [4] (see Figure 1). Modern neutron-based techniques span many orders of magnitude in required flux and energy range, including fundamental physics (FP), condensed-matter research, non-destructive testing, medical applications such as Boron Neutron Capture Therapy (BNCT), and emerging concepts for accelerator-driven subcritical systems (ADS). This diversity of usages highlights a clear mismatch between demand and availability, and calls for neutron sources that are not only intense, but also flexible and more accessible.

To address this, significant effort over the past decade has been devoted to the development of the so-called Compact Accelerator-driven Neutron Sources (CANS) [5, 6]. These facilities are explicitly designed to bridge the gap between large-scale installations and isotopic sources, typically targeting neutron source rates in the range 10^{12} – 10^{14} n/s. While a variety of design concepts have been explored, the vast majority of existing and proposed CANS rely on charged-particle beams impinging on a solid conversion target. As a result, their performance is ultimately constrained not by accelerator technology, but by the ability of the target to withstand intense energy deposition.

Proton-driven CANS, using low-energy protons (<100 MeV) on lithium or beryllium targets, represent the most mature technology in the compact-class. While these systems benefit from the favorable yields of (p, n) reactions, they face fundamental reliability challenges. Protons deposit energy volumetrically via ionization, creating intense Peak Energy Deposition Densities (PEDD) at the Bragg peak. This generates severe thermo-mechanical stresses that necessitate complex engineering solutions, such as rotating targets or liquid-metal cooling loops. These constraints limit the operational proton-CANS to beam powers to tens of kW [7], preventing straightforward scaling toward higher neutron production rates. Beyond these thermal issues, target longevity is also compromised by material degradation. As detailed by Lai and Yang [8], the accumulation of reaction by-products (e.g., hydrogen and helium) leads to blistering and radiation-induced swelling. This mechanism imposes a strict upper limit on the useful life of the target, estimated at approximately 1400 hours for a typical 21 kW beryllium target [8]. Furthermore, the operational stability of high-current proton drivers is often limited by frequent beam trips, preventing the delivery of the continuous, uninterrupted flux required for many applications [6].

Electron-driven photonuclear sources constitute a natural alternative [8]. Electron LINACs (eLINACs) are widely available, operationally robust, and supported by a mature industrial supply chain. Ridikas *et al.* [9] have shown in a comparative analysis that, although electron-driven systems are less efficient than spallation sources in terms of neutrons produced per unit beam energy, they offer advantages in reliability, compactness, and

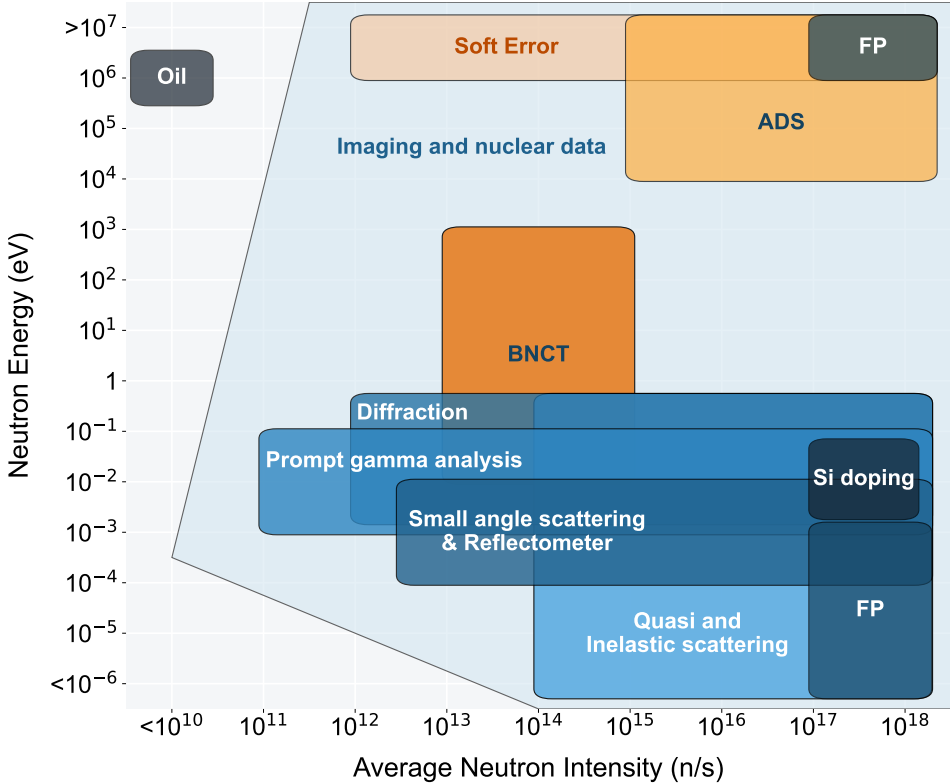


Figure 1: Classification of neutron sources and their application domains based on neutron intensity. Data adapted from [4]. FP = Fundamental Physics; BNCT = Boron Neutron Capture Therapy; ADS = Accelerator Driven Systems.

overall cost for neutron source rates below 10^{16} n/s. Consequently, photonuclear sources have been widely investigated for applications requiring moderate neutron intensities.

Nevertheless, conventional LINAC-based photonuclear sources remain subject to a fundamental limitation analogous to that of proton-driven systems, particularly with respect to thermal load management. The vast majority of eLINACs operate in pulsed mode, which is more stringent from a thermal management point of view than continuous operation, as short and intense pulses can induce large instantaneous energy deposition, leading to thermal shocks, mechanical stress, and fatigue damage in the irradiated materials. In standard configurations, high-energy electrons impinge on a high- Z converter (typically tungsten or tantalum) to generate bremsstrahlung photons, which subsequently induce (γ, xn) reactions in a secondary target [10]. This two-step process is intrinsically *inefficient*: only a small fraction of the electron beam power is converted into useful photons, while the majority is deposited as heat within the converter itself. As recently quantified by Herrador *et al.* [11], system configurations must therefore be designed to ensure acceptable peak energy deposition densities, typically expressed in J/g, in order to prevent instantaneous damage and limit thermo-mechanical degradation of the materials.

As a consequence, the performance of existing electron-driven CANS is severely restricted. Operational facilities such as GELINA, HUNS, KURRI-LINAC, and the Bariloche LINAC are confined to beam powers below 10 kW, yielding neutron intensities between 3.0×10^{11} and 3.4×10^{13} n/s [11]. Even high-power outliers, such as KIPT [12, 13] which operates at electron beam powers approaching 100 kW, are not able to exceed neutron rates of

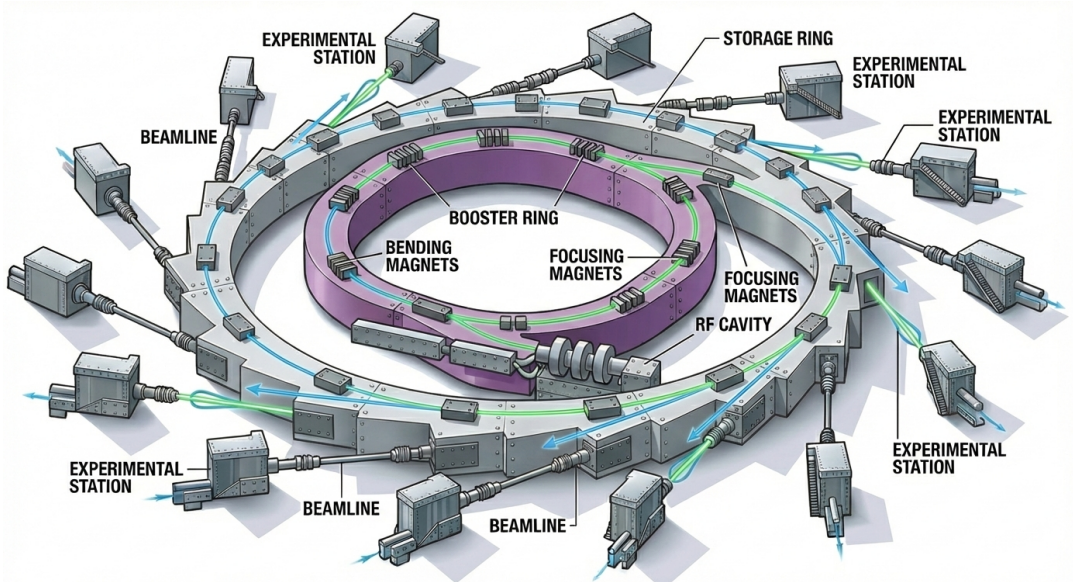


Figure 2: Illustrative example of a multi-beamline synchrotron-based facility, where a single storage ring feeds multiple photon beamlines.

approximately 3×10^{14} n/s. This establishes a technological limit that leaves the upper tier of the medium-intensity regime (i.e., 10^{14} – 10^{16} n/s) difficult to access for conventional photonuclear systems.

In this work, we propose a fundamentally different approach: a *synchrotron-driven photoneutron source*, here introduced as the **SYNERGY** concept (**S**Ynchrotron-driven **N**Eutron source for **R**esearch, energy **G**eneration and **t**herap**Y**). Starting from a preliminary analysis presented by the authors [14], the design exploits a storage ring to confine high-energy electrons in a closed orbit, where synchrotron radiation is continuously generated by bending magnets (S-BEND) or insertion devices. The emitted photon beam is extracted tangentially to the ring and transported toward an external neutron-production target. A schematic description of the synchrotron facility is shown in Figure 2.

The concept of neutron generation driven by synchrotron radiation is not new: it was explored in the 2000s, exploiting the SPring-8 facility [15] in Japan. Feasibility analyses were performed, first analytical [16] and then Monte Carlo based [17], aiming to evaluate the photoneutron yield from a beryllium target. In these works, the spectrum of the synchrotron radiation was mostly below the beryllium production threshold, namely the critical energy was close to 0.42 MeV, therefore without obtaining an efficient neutron generation with that concept. In our proposal the energy of the synchrotron is increased to reach the 10 MeV photons critical energy, allowing to re-evaluate the synchrotron capabilities as a neutron source [18].

The adoption of synchrotron radiation as a neutron driver represents a departure from current research trends, which are predominantly focused on compact accelerator-based sources [4, 6]. Rather than attempting to further scale single-beam LINACs or proton drivers toward increasingly challenging power densities, the synchrotron-based approach adopts a mature large-scale accelerator technology to overcome some of the intrinsic limitations related to power and thermal management identified in conventional CANS.

In contrast to pulsed operation, synchrotrons deliver radiation in an effectively continuous waveform (CW), significantly mitigating instantaneous energy deposition and reducing thermo-mechanical stresses on irradiated materials. From a conceptual standpoint, the key innovation of this design lies in decoupling the *particle deceleration* from *neutron generation*. In a storage ring, the photon beam is not generated by the electron beam impinging on a target that dissipates the whole power in a localized region; instead, it is directly generated by a bending magnet, and the lost energy is compensated by the RF system. The key advantage is that photon production does not rely on a material converter: the energy lost by the circulating electrons is *totally re-emitted* as synchrotron radiation (i.e., photons) and transported out of the ring. As a consequence, the neutron-production target interacts exclusively with the photon beam and is completely isolated from the primary charged-particle power.

This topological decoupling has some deep implications for target thermal management. Photons exhibit significantly longer interaction lengths and deposit far less energy per interaction than charged particles, leading to a drastic reduction in the specific heat load. Also, being the heat deposition continuous in time, the issues related to dynamical stress and fatigue may be neglected. The authors consider for the present analysis that a photon beam powers of 200 kW per beamline can be considered feasible without resorting to extreme or exotic engineering solutions, reducing the thermal bottleneck that constrains both proton-driven CANS and conventional LINAC-based photonuclear sources. Specific thermal analyses that verify this assumption will be addressed in a dedicated work.

Also, a synchrotron-based source inherently supports a *multi-usage* operational facility. A sufficiently large storage ring can simultaneously feed a large number of independent photon beamlines (on the order of several tens) distributed around the circumference of the accelerator. Multiple photoneutron stations can therefore operate in parallel, each optimized for a specific neutron spectrum or application, therefore improving the scientific impact and helping the cost-effectiveness of the facility compared to single-beam drivers. Within this framework, the ability of a synchrotron-driven photoneutron source is evaluated, understanding whether this system is able to address a broad set of application requirements (Figure 1).

This work represents the first milestone of the SYNERGY concept, in which the primary synchrotron photon beam is explicitly conceived as a driver for neutron production. The design and analysis of the photonuclear target therefore constitute natural first step in assessing the feasibility of this technology. In this context, a systematic parametric analysis is carried out to quantify the neutron source rate and energy spectrum achievable with different candidate target materials, namely uranium, tungsten, beryllium, and heavy water, which determine the range of applications supported by synchrotron-driven neutron sources. In fact, the availability of neutron source rates exceeding 10^{15} n/s opens new perspectives for accelerator-driven subcritical systems, while the flexibility in target material selection and geometric configuration enables tailoring of neutron spectra for diverse applications, including medical isotope production, soft-error testing of electronic components in space and high-altitude environments, and the generation of epithermal neutron beams suitable for BNCT.

The paper is organized as follows: Section 2 describes the adopted methodology, from the photonuclear production mechanisms to the simulation strategy; Section 3 presents the

simulation results in terms of integral photoneutron yield and yields resolved by energy range; Section 4 discusses the potential applications enabled by the obtained photoneutron yields; finally, Section 5 summarizes the main findings and draws concluding remarks.

2. Methodology

The design and optimization of a high-intensity photoneutron source driven by synchrotron radiation require a systematic evaluation of i) the interaction mechanisms between photons and matter, and ii) the possible geometric configurations of the conversion target. This section outlines the physical principles governing photonuclear production, the mathematical framework for calculating the neutron yield, and the simulation strategy adopted to define the optimal target dimensions.

2.1. Photon Source

As already pointed out we propose to use storage ring with multiple photon beamlines, each producing a MeV-range photon beam. More in detail, the storage ring has an electron energy of 32 GeV, and, in the single beamline, the high-energy photon beam is emitted by a high-intensity (15 T) short dipole magnet [18]. The main parameters of the synchrotron are given in Table 1, while the energy distribution of the emitted synchrotron radiation, calculated using the SPECTRA code [19], is shown in Figure 3. For the synchrotron parameters, we have considered two possible configurations with different circulating currents: a 15 mA case and a 45 mA case. The second case requires an overall ring cavity voltage that is one third of that in the 15 mA case, but also a shorter 15 T radiating magnet [20]. In terms of stored current, the 45 mA case is very similar to that of the HERA electron ring [21]. The final configuration and design of the accelerator must take into account several aspects, such as beam stability and quantum lifetime [20], however, the fact that we can consider different beam current configurations that have already been achieved in previous large colliders provides significant margins for its design and optimization. For the application in SYNERGY it is of interest to use a very high, but still technically feasible magnetic field B for the photon source to obtain photon energies E_γ of the same order as typical GDR excitation energies, while keeping the electron energy E_e and therefore the size of the synchrotron in a reasonable range. E_γ scales in proportion to $E_e^2 \cdot B$. To achieve a 15 T dipole field in a magnet with a sufficient opening for the circulating electron beam and for the extraction of the photon beam we assume a split solenoid design based on high temperature superconductor (HTS) coils.

The achievable total photon source intensity in a single beamline is $S_\gamma = 2.02 \times 10^{17} \gamma/\text{s}$ in the range 1 MeV - 37 MeV, corresponding to a total photon beam power of approximately 200 kW. As already pointed out in Section 1, a key advantage of this relatively large synchrotron is the ability to generate multiple photon beams from independent beamlines, enabling separate operation and power supply to multiple reactors simultaneously. The number of beamlines in the synchrotron is directly related to its circumference: a larger circumference allows for a greater number of beamlines to operate independently. Additionally, increasing the synchrotron's circumference reduces the required curvature radius for conventional magnets, which lowers their power consumption and simplifies the overall machine design. The detailed design of the synchrotron itself and the HTS magnet will be addressed in a forthcoming publication.

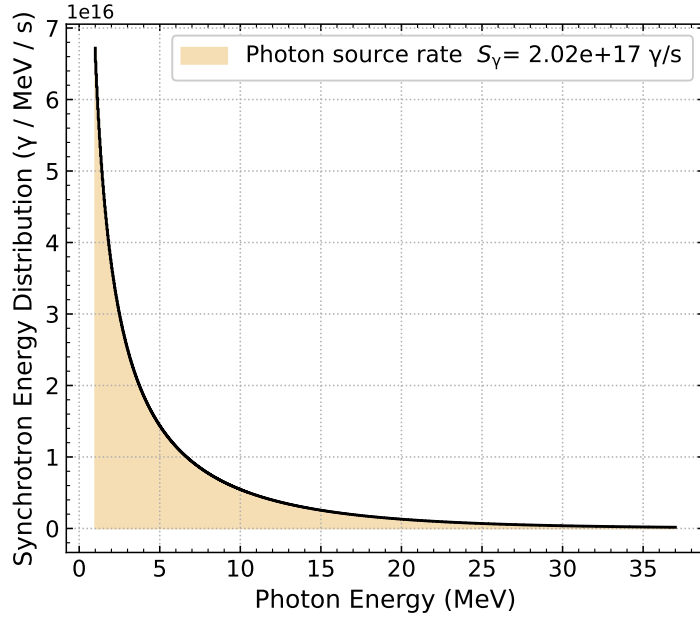


Figure 3: Energy distribution of the incident synchrotron radiation considering a beam power of 200 kW. The total source rate in the energy range 1-37 MeV is evaluated to be $2.02 \times 10^{17} \gamma/s$

Parameter	Value
Energy (GeV)	32
Beam current (mA)	15(45)
Radiating dipole magnet field (T)	15
Radiating magnet length (cm)	5(1.7)
Ring total length (km)	5
Number of photon beamlines (-)	50
Synchrotron power per beamline (kW)	200
Number of photons per beamline (γ/s)	2.02×10^{17}
Photon energy extremes (MeV)	1-37

Table 1: Main parameters of the electron synchrotron (in parenthesis the case with 45 mA circulating current).

2.2. Mechanism of Photonuclear Reactions

Unlike proton-based sources, where either high-energy protons directly disintegrate nuclei (in the spallation scenario) or neutrons are generated through stripping processes (if (p, n) reactions), electron-driven systems typically operate through a two-step conversion process [10]. In conventional systems (like e-CANS, for instance), electrons first impinge on a high-Z converter to generate Bremsstrahlung photons, which subsequently interact with nuclei to produce neutrons. In the proposed synchrotron-driven concept, the first step is inherently decoupled: high-energy photons are emitted by electrons circulating in the storage ring as they are deflected by dipole magnets, and are subsequently transported to the beamline through dedicated photon extraction ports. Consequently, the interaction of interest occurs directly between the incident synchrotron photon beam and the target nuclei, inherently increasing the efficiency being a *single-step process*.

It is fundamental to emphasize that photonuclear reactions represent only a small subclass of photon interactions with matter. The most probable interaction mechanisms in the energy range of interest (\sim 1-40 MeV) are photoatomic processes, namely *Compton scattering* and *electron-positron pair production*. For most materials, the photonuclear cross-section contributes less than 2-3% to the total photon attenuation coefficient. Photonuclear targets may be categorized into two distinct classes, based on their atomic number:

- **Low-Z converters** (e.g., Deuterium, Beryllium): as shown in the top panel of Figure 4, these materials are characterized by very low photoneutron threshold energies (2.22 MeV for deuterium, 1.67 MeV for beryllium) and relatively small cross-sections (in the millibarn range). For these light nuclei, the dominant competing photoatomic interaction is Compton scattering. However, as highlighted by Fynan *et al.* [22] for deuterium, Compton scattering allows the target to effectively "re-use" photons: a scattered photon emerging with energy above the threshold can still induce a photoneutron reaction.
- **High-Z converters** (e.g., Tantalum, Uranium): the bottom panel of Figure 4 shows the cross-sections for Tantalum (^{181}Ta) and Uranium (^{238}U) photonuclear interactions. These materials exhibit massive Giant Dipole Resonance (GDR) peaks in the 10-20 MeV range [10, 23, 24], with magnitudes reaching hundreds of millibarns (note the difference in scale compared to the top panel). However, their efficiency is penalized by the pair production process, which acts as a dominant absorption mechanism within this energy range. Adopting an actinide converter (e.g., uranium) instead of a heavy-metal target (e.g., tantalum) inherently increases photoneutron production, as actinides provide a larger number of available reaction channels. In addition to single-neutron emission via (γ, n) , there is also the $(\gamma, 2n)$ channel and, most importantly, photofission (γ, F) . Photofission enhances the total neutron yield by releasing multiple neutrons per event: for ^{238}U , the average neutron multiplicity increases almost linearly with photon energy, reaching approximately 2.5 for 6 MeV photons and about 4.0 for 18 MeV photons. This behavior is attributed to second-chance fission, which becomes accessible for photon energies above the second-chance threshold (around 12 MeV). Further details can be found in the pioneering measurements by Caldwell *et al.* [24] and in the recent review by Filipescu *et al.* [25]. Overall, these mechanisms provide actinides with a distinct advantage over non-fissile high- Z targets such as tantalum.

It is crucial to acknowledge that the accuracy of calculations involving photonuclear interactions strongly depends on the quality of the evaluated nuclear data libraries employed. A recent critical review by Sari [26], together with subsequent benchmark studies [27, 28], has identified systematic discrepancies among the major photonuclear data libraries. In particular, the widely used ENDF7u photonuclear library (distributed within several evaluated data releases, such as ENDF/B-VII.1 and ENDF/B-VIII.0), which serves as the default option for many Monte Carlo codes including MCNP and OpenMC, has been shown to consistently underestimate photonuclear cross-sections when compared with the IAEA/PD-2019 [29] and JENDL-5 [30] reference libraries, as well as with experimental data. As highlighted in the review, this bias typically appears as an underestimation of the peak cross-section values in the Giant Dipole Resonance (GDR) region and in a mismatch in the low energy threshold. The discrepancy is systematic

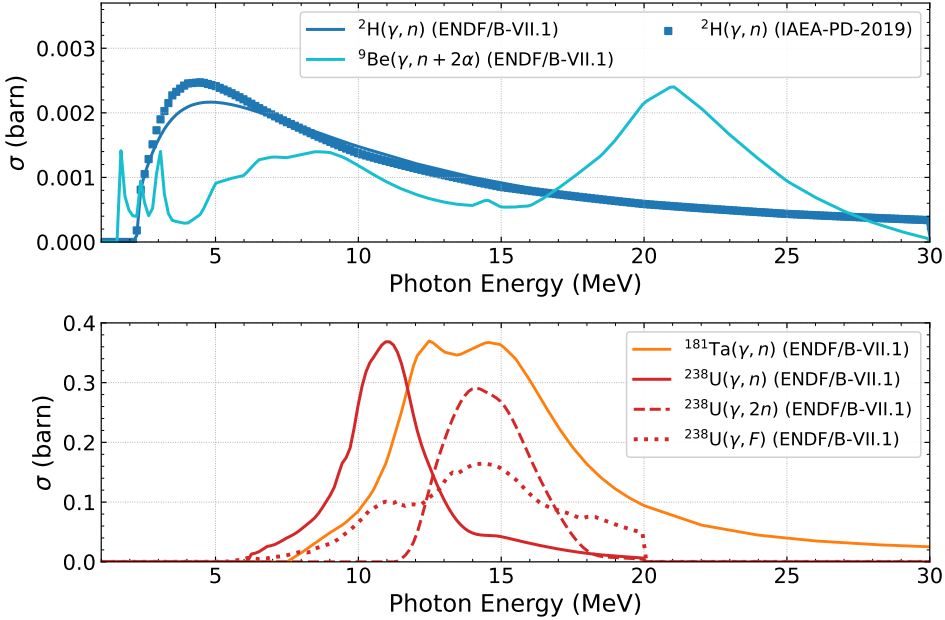


Figure 4: Photonuclear cross-sections for representative Low- Z and High- Z isotopes. **Top Panel:** Low- Z isotopes (Deuterium and Beryllium) characterized by low threshold energies. The plot highlights the discrepancy for the ${}^2\text{H}(\gamma, n)$ reaction between the standard ENDF/B-VII.1 library (dashed line) and the JENDL-5 library (solid line) as reviewed in [26]. **Bottom Panel:** High- Z isotopes (Tantalum and Uranium) dominated by the Giant Dipole Resonance (GDR). For ${}^{238}\text{U}$, the specific contributions of (γ, n) , $(\gamma, 2n)$, and photofission (γ, F) channels are explicitly shown. These data are in very good agreement with experimental measurements from Caldwell *et al.* [24]

and affects both high- Z materials (such as tungsten and tantalum) and low- Z materials (such as deuterium). As a consequence, simulations relying on this library tend to predict photoneutron production rates that are lower than experimental observations by amounts ranging from a few percent up to factors of 2–3 [26]. To date, uranium photonuclear data show good agreement with experimental measurements; however, a similar underestimation cannot be excluded for actinides. In this work, despite the known inconsistencies affecting a large fraction of the nuclides, the ENDF/B-VII.1 [31] photonuclear data library is adopted across all the simulation codes (i.e., MCNPX, OpenMC, and FLUKA). This choice is primarily motivated by the limited availability of newer, corrected libraries across the full set of simulation tools employed, whereas the ENDF series remains the most accessible and widely supported option. Consequently, the simulation results presented in this study are subject to an intrinsic *systematic negative bias*, and should therefore be interpreted as *conservative lower bounds* on the true production capabilities of the facility.

2.3. Photoneutron Yield and Neutron Source Rate

The key figure of merit for the primary source performance in producing neutrons is the photoneutron yield (Y_n), defined as the total number of neutrons produced per unit of incident photon, n/γ . Assuming the target is sufficiently thick to interact with the entire incident photon flux, and that all the photons interact only once with the target, Y_n may be generalized from the formula reported in [16] by combining all the reaction cross-sections over the incident photon energy spectrum. The analytical expression for the yield is given by:

$$Y_n = \int_0^\infty \frac{d\chi_\gamma}{dE_\gamma} \underbrace{\left(\frac{\sigma_{\gamma,n}(E_\gamma)}{\sigma_{tot}(E_\gamma)} + 2 \frac{\sigma_{\gamma,2n}(E_\gamma)}{\sigma_{tot}(E_\gamma)} + \nu_{\gamma,F}(E_\gamma) \frac{\sigma_{\gamma,F}(E_\gamma)}{\sigma_{tot}(E_\gamma)} + \dots \right)}_{w(E_\gamma) = \text{photoneutron production probability}} dE_\gamma \quad (1)$$

where:

- $d\chi_\gamma/dE_\gamma$ represents the spectrum of the incident photon beam (in this scenario, the synchrotron radiation spectrum). Figure 3 presents the synchrotron distribution times the source intensity used in this study, namely $S_\gamma \cdot \frac{d\chi_\gamma}{dE_\gamma}$. This distribution is characterized by a high intensity in the low-energy range and a tail extending up to 40 MeV, covering the entire GDR region;
- σ_{tot} is the microscopic total photon cross-section;
- $\sigma_{\gamma,n}$, $\sigma_{\gamma,2n}$, and $\sigma_{\gamma,F}$ are the microscopic cross-sections for single neutron emission, double neutron emission, and photofission, respectively;
- $\bar{\nu}_{\gamma,F}$ is the average number of neutrons emitted per photofission event.

This formulation allows for a direct analytical evaluation of the neutron production across different materials by weighting their cross-sections against the synchrotron spectrum. However, it strictly quantifies the generation per unit of incident photon, and does not account for the subsequent transport of neutrons within the target volume, nor does it consider self-absorption or scattering effects. To provide a comprehensive analysis that inherently incorporates these secondary physical phenomena and geometric effects, Monte Carlo simulations were adopted. Thus, the evaluation of the photoneutron yield is computed as:

$$Y_n = \frac{1}{N_\gamma} \sum_{i=0}^{N_\gamma} \xi_i \quad (2)$$

Where N_γ is the number of photon histories simulated and ξ_i is the number of neutrons that cross a control volume that envelope the target. The following subsections are devoted to both overview the tools adopted and specify the simulation setup and optimization strategy.

It is important to highlight that the absolute *neutron source rate* S_n , defined as the number of neutrons per second that leave the target, may be evaluated from the product between the photoneutron yield Y_n (n/γ) and the photon source rate S_γ (γ/s). This value is of key importance for comparing different technologies, since it represents the facility's global performances.

2.4. Computational Tools

The characterization of the photoneutron source relies on *fixed-source simulations*, where the synchrotron radiation beam is defined as an external photon source impinging on the target. This approach allows for the direct evaluation of the photoneutron flux distributions, reaction rates, and energy spectra generated by the interaction of the incident photons with the converter material. To ensure the reliability and consistency of the results, the analysis was performed using a multi-code approach involving three independent Monte Carlo transport codes: OpenMC, MCNPX, and FLUKA.

The primary optimization analysis was conducted using the OpenMC code. Specifically, this work utilized a development branch implemented by [32], which integrates advanced photonuclear physics capabilities into the standard solver. This version allows for the explicit transport of photons and the generation of secondary neutrons using tabulated cross-section data, making it suitable for high-fidelity simulations. Since this version represents an unofficial branch, the authors performed a verification of the code capabilities using the broomstick problem as a benchmark case [33].

To further verify the accuracy of the OpenMC predictions, the systems were independently replicated and simulated using MCNPX (version 2.7) [34]. MCNPX is a well-established standard in nuclear engineering for multiparticle transport and features built-in functionality for photonuclear physics. In these simulations, the synchrotron spectrum was implemented using the SDEF card to define the external photon source distribution.

Finally, the general purpose FLUKA code [35] (version 4-5.0) was employed as a third cross-comparison tool. Renowned for its accuracy in handling complex interaction physics and shielding problems, FLUKA provided an additional layer of validation for the neutron flux distributions and yield calculations, ensuring that the physical modeling of the photon-matter interactions was consistent across different transport algorithms. Here, the synchrotron photon source distribution was implemented using the source_newgen.f routine.

2.5. Simulation Strategy and Target Optimization

The optimization of the photoneutron source configuration was driven by a systematic parametric analysis aimed at maximizing the neutron yield per incident particle (n/γ). The simulation strategy was designed to decouple the geometric optimization from the final characterization, ensuring both computational efficiency and high statistical confidence in the reported performance metrics.

2.5.1. Geometric Parametrization

To determine the optimal dimensions for each candidate converter, the target geometry was modeled as a cylinder defined by two independent variables: the radius (R) and the length (L), as illustrated in Figure 5. The parametric sweep investigates two competing physical effects:

- **Saturation:** the variation of the length L identifies the saturation thickness, defined as the point where the production of additional photoneutrons is balanced by the self-shielding (absorption) and leakage of the generated neutron population.
- **Indirect absorption:** the variation of the radius R is critical to optimize the neutrons generated by scattered photons and the one absorbed by the target. In fact, a sufficiently large radius is able to capture secondary off-axis photons generated by Compton scattering and electromagnetic showers, which would otherwise escape laterally without inducing photonuclear reactions. On the other hand, the excessively large radius increases the probability of neutron absorption within the target volume, thus reducing the overall yield.

The incident synchrotron beam was modeled as a point source aligned with the cylinder axis. This assumption isolates the intrinsic attenuation properties of the material (namely, the photon mean free path and neutron cross-section) from the specific spatial profile of

the beamline. Consequently, the optimal R and L values derived in this way represent the ideal physical dimensions of the target volume.

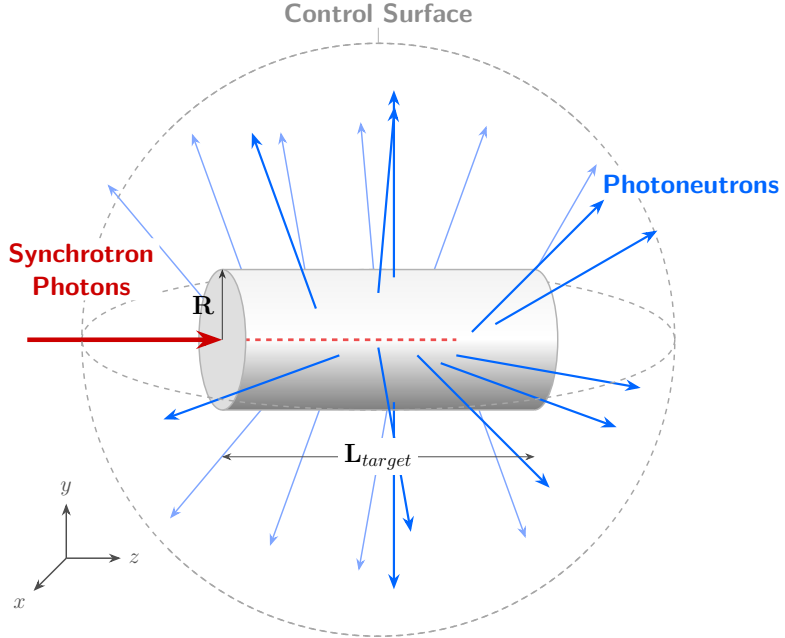


Figure 5: Schematic representation of the cylindrical target geometry used for parametric optimization.

2.5.2. Material Selection

To assess the system versatility across different application domains, several target materials were selected for optimization. These are categorized based on their dominant interaction mechanisms (as detailed in Table 2).

The rationale for this selection includes:

- **Moderating Materials** (D_2O , Be, BeO): Low-Z targets capable of producing naturally moderated spectra (thermal/epithermal) for BNCT and scattering science, leveraging the high photon survival probability in Compton scattering.
- **Heavy Metals** (U_{nat} , W_{nat} , Ta): Selected to maximize neutron yield through the (γ, xn) and photofission (for fissile isotopes), which is essential for high-flux applications such as Accelerator Driven System (ADS) driving and isotope production.

2.5.3. Computational Workflow

The numerical analysis was performed in a two-stage process to optimize the computational resources while ensuring high accuracy for the final design points:

1. **Parametric Sweep:** a broad scan of the R - L parameter space was performed using OpenMC. To efficiently identify the maximum yield region for each material, these simulations were run with a statistical population of 10^7 primary particles. This sample size was sufficient to find relative trends and locate the optimal geometric maxima.
2. **High-Fidelity Characterization:** once the optimal dimensions (R_{opt} , L_{opt}) were identified for each material, a second set of simulations was performed to precisely

Table 2: Composition and properties of the simulated target materials.

Target	Isotope	Atomic fraction (%)	Density (g/cm ³)
Be	⁹ Be	100	1.8
BeO	⁹ Be	50	3.0
	¹⁶ O	50	
D ₂ O	² H	66.7	1.10
	¹⁶ O	33.3	
U _{nat}	²³⁴ U	5.4E-3	19
	²³⁵ U	0.7204	
	²³⁸ U	99.2742	
W _{nat}	¹⁸² W	26.5	19.3
	¹⁸³ W	14.3	
	¹⁸⁴ W	30.6	
	¹⁸⁶ W	28.4	
Ta	¹⁸¹ Ta	100	17

quantify the source performance. In this phase, the optimal configurations were simulated using all three codes (OpenMC, MCNPX, and FLUKA) with a high-statistics population of 10^8 primary particles. This step ensured that the final reported yields, spectra, and reaction rates are statistically robust and cross-validated among the different transport solvers.

3. Simulation Results

This section shows the computational results of the SYNERGY target analysis. First, the identification of the geometric optimal values for each target material is presented; then, the spectral characterization and cross-code validation of the optimal configurations are performed; finally, the evaluation of the absolute neutron production rates is presented.

3.1. Geometric Optimization

The parametric sweep performed with OpenMC (10^7 photon histories) allowed for mapping of the photoneutron yield (Y_n) as a function of target radius (R) and length (L). The resulting yield contours are shown in Figure 6, where the marker **M** indicates the configuration that maximize the total photoneutron generation.

The analysis reveals a distinct physical behavior governing the optimal dimensions, driven by the competition between photon attenuation and neutron transport:

- **High-Z Materials** (U_{nat}, W_{nat}, Ta): these targets exhibit a rapid saturation of the neutron yield. Due to the high density and large macroscopic photonuclear cross-sections, the incident photon beam is fully attenuated within a relatively short

path. Consequently, the optimal dimensions are compact, with lengths of the order of 10-25 cm. Increasing the volume beyond this saturation point does not enhance production but introduces negative self-shielding effects (i.e., neutron absorption).

- **Low-Z Materials (D_2O , Be, BeO):** conversely, moderators require significantly larger volumes to approach saturation. The maxima are found at lengths exceeding 2 meters and radii up to 50 cm. This is attributed to the longer mean free path of photons (dominated by Compton scattering) and the necessity to minimize the leakage of neutrons, which undergo extensive scattering and moderation within the target bulk.

The identified optimal dimensions (R^{opt} , L^{opt}) and the corresponding maximum yields are summarized in Table 3. These geometric values are adopted as the fixed reference design for the subsequent energy distribution analysis.

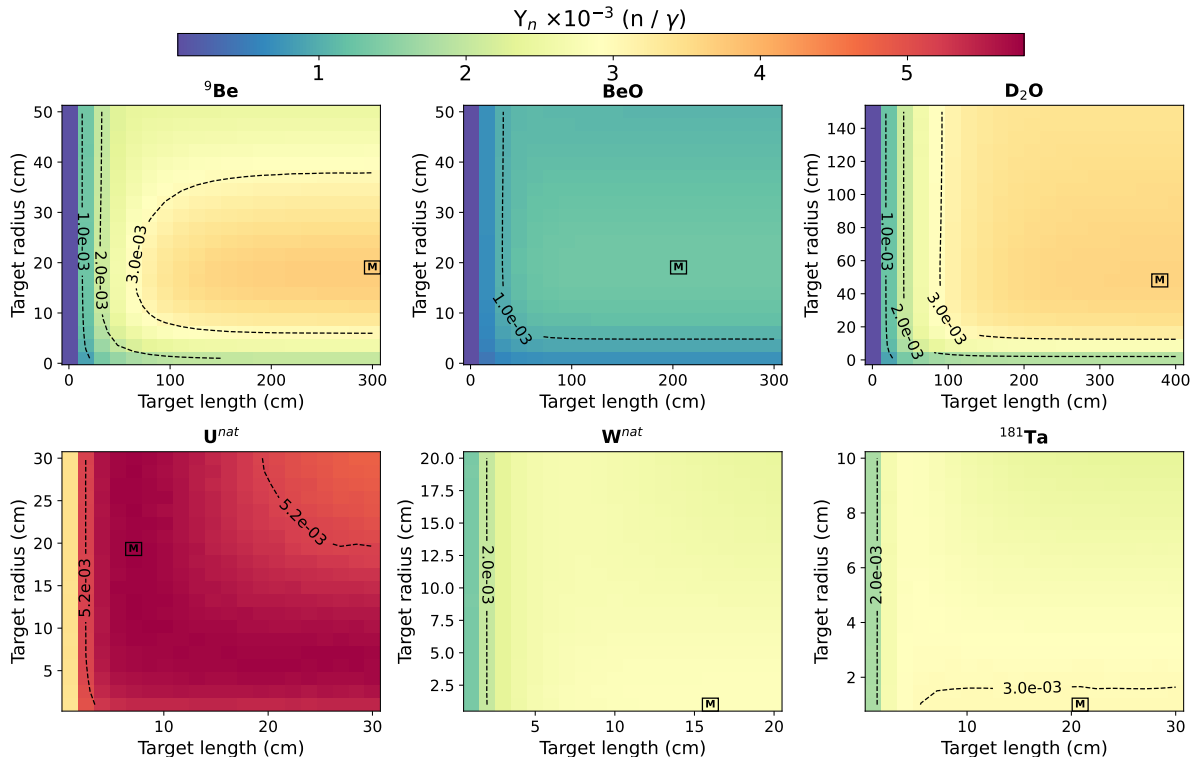


Figure 6: Photoneutron-yield scan over target radius and length for all materials. The color scale indicates the magnitude of Y_n (neutrons/source photon), and the marker **M** indicates the optimal geometric configuration.

3.2. Spectral Analysis and Cross-Code Validation

Using the optimal dimensions listed in Table 3, high-statistics simulations (10^8 photon histories) were performed to characterize the neutron energy spectra emitted from the targets. Figure 7 presents the comparison of the neutron energy distribution calculated by OpenMC, MCNPX, and FLUKA in the optimal configuration. The results show that the emitted energy distribution naturally separate into two distinct categories. The high-Z targets (U, W, Ta) emit a predominantly fast spectrum (peaked between 0.1 and 1 MeV), typical of evaporation neutrons produced by (γ, xn) and photofission reactions with minimal in-target moderation. In contrast, the low-Z targets (D_2O , Be and BeO) exhibit

Table 3: Optimal photoneutron yields and target dimensions resulting from the geometric sweep. Data from OpenMC with 10^7 photon histories.

Target	$Y_n^{\text{opt}} (\text{n}/\gamma)$	$R^{\text{opt}} (\text{cm})$	$L^{\text{opt}} (\text{cm})$
${}^9\text{Be}$	$(3.703 \pm 0.002) \times 10^{-3}$	19.05	300.00
BeO	$(1.297 \pm 0.001) \times 10^{-3}$	19.05	205.58
D_2O	$(3.618 \pm 0.001) \times 10^{-3}$	48.05	379.00
U_{nat}	$(5.792 \pm 0.011) \times 10^{-3}$	19.32	7.11
W^{nat}	$(2.865 \pm 0.003) \times 10^{-3}$	1.00	16.00
${}^{181}\text{Ta}$	$(3.029 \pm 0.002) \times 10^{-3}$	1.00	20.84

a pronounced thermal and epithermal component, confirming that for these materials, the target acts simultaneously as a converter and a moderator. In each subplot there is also present a chart that reports the total neutron yield, evaluated as the sum of the histogram bins. The total magnitude appears to be consistent across the three codes, with relative differences always below 10 % except the case of ${}^9\text{Be}$, where the comparison OpenMC-FLUKA shows a $\sim 20\%$ difference.

To further quantify the agreement between the three codes, the ratio of the neutron energy distribution obtained with MCNPX and FLUKA relative to OpenMC is shown in Figure 8. The ratio is showed in the energy interval where the flux values are significant (i.e., above $1 \times 10^{-5} \text{ n}/\gamma/\text{bin}$) to avoid artifacts due to the low magnitude in the tails of the spectra. The comparison shows that MCNPX and OpenMC are in very good agreement across the entire energy range, with deviations below within $\pm 5\%$, except for BeO target where there is present an almost constant bias of $+10/15\%$, and Tantalum where there is an oscillating pattern that stays always below $\pm 40\%$. On the other hand, the comparison OpenMC-FLUKA present similarities in the moderating targets, showing a non linear trend for thermal energies, then stabilizing in the epithermal region to a ratio that goes from $+20\%$ for ${}^9\text{Be}$ up to -5% for heavy water. High-Z converters show larger discrepancies, with FLUKA showing a decreasing trend for Uranium and a non linear trend for tungsten and Tantalum. These differences could be ascribed to the fact that the particle transport in FLUKA mixes photonuclear data libraries and models, whereas both MCNPX and OpenMC relies solely on nuclear data.

3.3. Absolute Production Rates and Energy Distribution

To evaluate the realistic source capability, the calculated yields were normalized to the nominal synchrotron beam power of 200 kW, corresponding to an incident photon source rate for a single beamline of $2.02 \times 10^{17} \gamma/\text{s}$ in the range 1-37 MeV.

Table 4 summarizes the absolute neutron source rates (n/s) for each optimized target. To facilitate the comparison with application requirements in the next section, the neutron intensities has been decomposed into three standard energy groups:

- Thermal Flux ($< 1 \text{ eV}$): relevant for scattering and capture therapies.
- Epithermal Flux ($1 \text{ eV} - 100 \text{ keV}$): critical for clinical BNCT requirements [36].
- Fast Flux ($> 100 \text{ keV}$): the driving component for subcritical multiplication and materials testing.

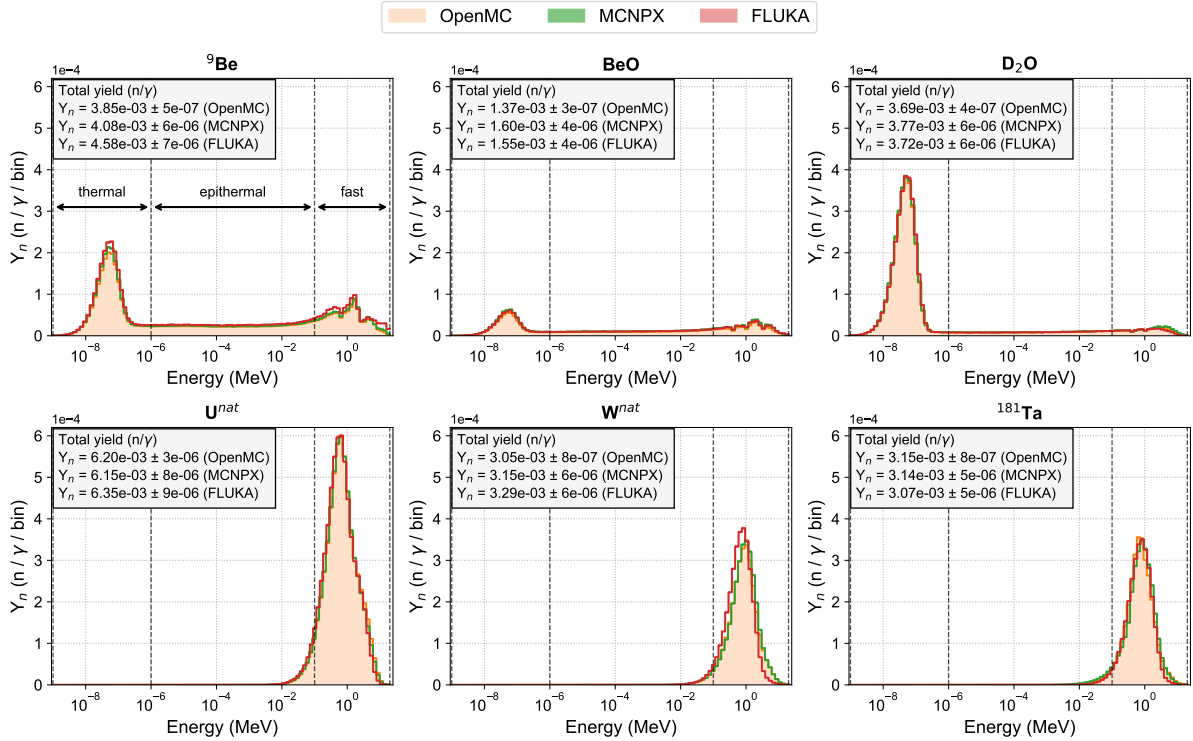


Figure 7: Comparison of neutron energy distribution for the optimal target geometries using OpenMC, MCNPX, and FLUKA. The total photoneutron yield is reported in the dedicated chart for each code.

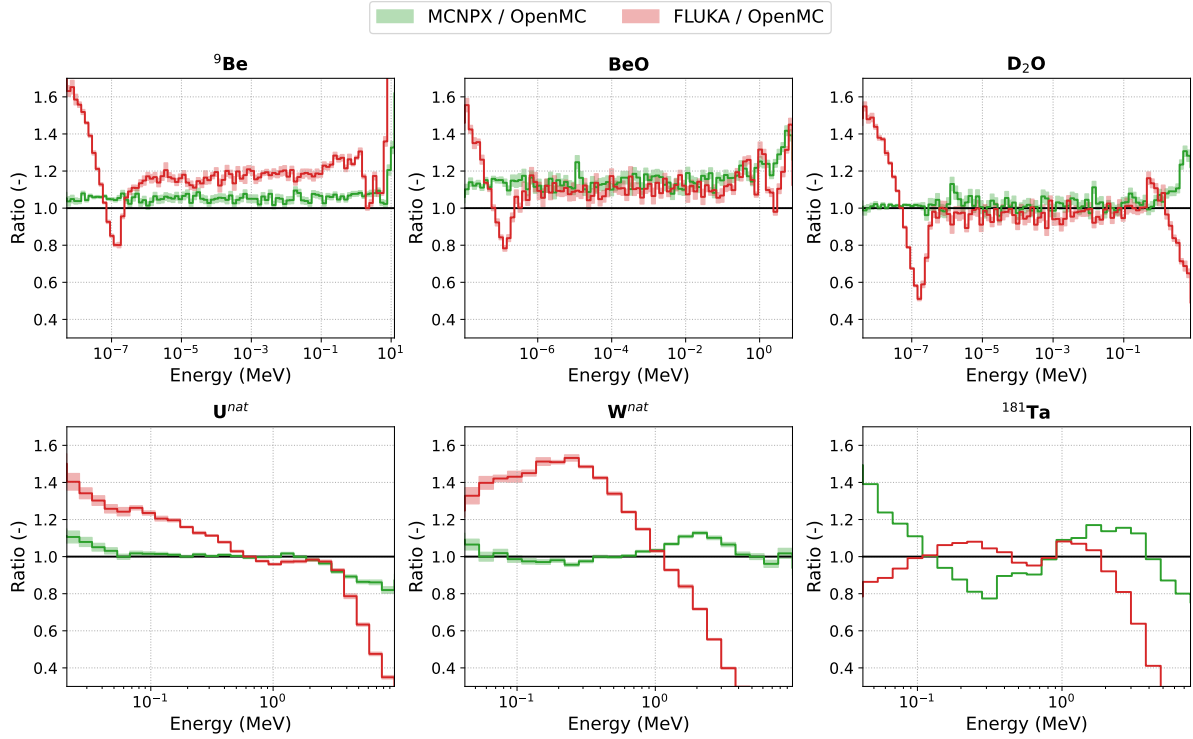


Figure 8: Ratio of neutron energy distribution obtained with MCNPX and FLUKA relative to OpenMC for the optimal target geometries.

The data indicates that Uranium-based target provides the highest integral source strength, exceeding 1×10^{15} n/s, while Beryllium and Deuterium targets, despite a lower total yield, offer intrinsic thermal/epithermal intensities in the range of $1-6 \times 10^{14}$ n/s. The detailed benchmarking of these values against existing facilities and their suitability for specific industrial and medical use-cases are discussed in Section 4.

Table 4: Photoneutron source rate S_n produced by different target materials, normalized to the expected synchrotron photon source rate ($S_\gamma = 2.02 \times 10^{17}$ γ/s), and subdivided into thermal, epithermal, and fast neutron energy groups. The data comes from OpenMC simulation, with 10^8 histories. Only average values are reported for sake of simplicity, being the uncertainty $< 0.5\%$.

Material	Thermal S_n (n/s) [1 meV, 1 eV]	Epithermal S_n (n/s) [1 eV, 0.1 MeV]	Fast S_n (n/s) [0.1 MeV, 20 MeV]	Total S_n (n/s) [1 meV, 20 MeV]
⁹ Be	3.6×10^{14}	2.3×10^{14}	1.9×10^{14}	7.8×10^{14}
BeO	1.0×10^{14}	9.7×10^{13}	7.6×10^{13}	2.8×10^{14}
D ₂ O	6.0×10^{14}	8.8×10^{13}	5.6×10^{13}	7.4×10^{14}
U _{nat}	$\leq 1.0 \times 10^7$	6.3×10^{13}	1.2×10^{15}	1.3×10^{15}
W _{nat}	$\leq 1.0 \times 10^7$	2.1×10^{13}	6.0×10^{14}	6.1×10^{14}
¹⁸¹ Ta	$\leq 1.0 \times 10^7$	2.3×10^{13}	6.1×10^{14}	6.4×10^{14}

4. Discussion: Application Range and Comparison with Literature

The simulation results presented in Section 3 demonstrate that the SYNERGY concept offers a highly versatile system, capable of addressing a broad spectrum of neutron fields (and, therefore, of applications) through the strategic selection of target materials. The authors propose within this section, four applications where the SYNERGY concept could be adopted. To assess the potentialities of this kind of system, the comparison of the simulated neutron intensities is pursued against both the theoretical requirements for key applications and the performance of reference facilities, that can be considered state-of-the-art. In particular, we focus on both reactor sources as well as accelerator-driven sources (i.e., Spallation, CANS-p and CANS-e). A comprehensive overview may be found in Table 5, while the following paragraphs are dedicated to single applications.

ADS. In subcritical reactors the neutron source represents the key element to maintain the fission chain able to either produce power or dedicated to transmutation of minor actinides. The required source strength depends on the specific ADS design, including the desired power level, subcriticality, and fuel composition, but typically ranges from 10^{14} to 10^{17} n/s for experimental and demonstration reactors [37, 38].

At the high-intensity frontier, spallation technology is represented by MYRRHA (Belgium), a large-scale infrastructure utilizing a 600 MeV proton beam on a Lead-Bismuth Eutectic (LBE) target to generate a massive neutron rate of $\sim 2 \times 10^{17}$ n/s, suitable for industrial transmutation and high-flux research [38, 39]. On the compact scale, the CANS-p category is represented by CPHS (China), which plans to employ a low energy 13 MeV beam on a ⁹Be target for an intensity of $\sim 1 \times 10^{13}$ n/s [40], while the CANS-e category is represented by KIPT (Ukraine), using a 100 kW electron LINAC on a Uranium target to reach $\sim 3.0 \times 10^{14}$ n/s [12, 13]. In this context, SYNERGY emerges as a high-performance intermediate solution, achieving a total neutron intensity of 1.3×10^{15} n/s from a single beamline through the use of a natural uranium target. When extrapolated to the full synchrotron configuration comprising 50 beamlines, the total neutron source intensity

may reach up to 6.5×10^{16} n/s. This performance represents a substantial improvement over standard compact proton- and electron-driven reference facilities, effectively bridging the gap between accessible laboratory-scale sources and large spallation research centers.

Isotope Production. Beyond ADS studies, the high photon and neutron source intensity achievable with synchrotron-driven sources open an application domain in radioisotope production. Depending on the selected operating mode, the proposed facility can either act as a neutron source, via photon-to-neutron conversion, or directly exploit the primary synchrotron photon beam for photonuclear reactions. In the latter configuration, radioisotopes are produced through (γ, n) or (γ, p) reactions directly in the production target, bypassing the intermediate neutron conversion stage. This approach is currently being industrialized for the supply of ^{99}Mo , the parent isotope of $^{99\text{m}}\text{Tc}$ used in nuclear medicine, within the framework of the Lighthouse project [41]. Similar photonuclear pathways have been proposed for other medically and industrially relevant isotopes, including ^{64}Cu , ^{67}Cu , ^{68}Ge , and ^{186}Re [42, 43].

From a broader perspective, radioisotope production technologies are most consistently compared when organized by reaction channel. For neutron-capture production via (n, γ) reactions, the relevant figure of merit is the neutron flux or neutron source rate available at the irradiation position. Research and multipurpose reactors routinely deliver thermal neutron flux in the range 10^{13} – 10^{15} n/cm²/s, enabling large-scale production of isotopes such as ^{99}Mo , ^{131}I , ^{177}Lu , and ^{186}Re , and remain the dominant technology despite aging infrastructure and supply vulnerabilities [44, 45, 46]. Spallation sources achieve very high integrated neutron source strengths but are presently optimized for materials science rather than routine isotope production [6]. Compact accelerator-based neutron sources (CANS), based on low- to medium-energy proton beams on light-element targets, typically provide neutron fluxes up to 10^{12} – 10^{13} n/cm²/s, sufficient for demonstration-scale (n, γ) or $(n, 2n)$ production routes [47, 6]. Electron linacs and synchrotrons can also contribute indirectly to (n, γ) production through photoneutron fields generated by bremsstrahlung or synchrotron radiation, where neutron intensities of order 10^{13} n/s have been reported for kilowatt-class photon beams on high- Z converters [6, 48].

In contrast, direct photonuclear production via (γ, n) and (γ, p) reactions is governed by the available photon flux and by the spectral overlap with reaction thresholds and GDR peaks. Electron linacs using bremsstrahlung spectra have demonstrated the production of ^{99}Mo , ^{64}Cu , ^{67}Cu , ^{68}Ge , ^{177}Lu , and ^{186}Re with photon source rates of 10^{14} – 10^{15} γ/s and endpoint energies in the 30–40 MeV range [49, 48]. Synchrotron-based γ sources extend this concept by providing high-brightness, quasi-continuous or narrow-band photon beams with intensities up to 10^{17} γ/s in the GDR energy domain, enabling efficient photonuclear production with reduced target heating and improved spectral matching [50, 51, 52].

Within this framework, the results presented in this work position synchrotron-driven sources at the upper end of photonuclear performance. For each beamline, an expected photon source rate of $S_\gamma = 2.02 \times 10^{17}$ γ/s is achieved, while photon-to-neutron conversion on a UO_2 target yields neutron source strengths approaching 10^{15} n/s. These values are comparable to, or exceed, those reported for compact accelerator-based neutron sources and electron-linac-driven photoneutron systems, while remaining below large spallation facilities. Importantly, the synchrotron offers simultaneous access to both reaction channels, (n, γ) via photoneutron production and (γ, n) and (γ, p) via direct irradiation, within a single infrastructure. This dual-modality capability distinguishes synchrotron-based concepts as a complementary technology for isotope production, rather

than a direct replacement for reactor- or proton-driven routes.

Soft error testing. Soft error testing is a critical process for ensuring the reliability of modern electronics against environmental radiation. This necessity arises from high-energy cosmic rays interacting with the Earth’s atmosphere that generate showers of secondary particles, particularly neutrons. The resulting terrestrial neutron flux is characterized as a *white spectrum*, spanning continuously from thermal energies up to hundreds of MeV. However, the most dangerous reactions for semiconductors occur primarily in the MeV range [4]; in this regime, uncharged neutrons can penetrate device packaging and collide with silicon nuclei, triggering nuclear recoils and releasing charged secondary particles that cause localized ionization. This charge deposition can flip memory bits or disrupt logic states (Single Event Effects, SEE). To validate device reliability without waiting years for natural accumulation, engineers may use accelerated testing using a controlled neutron source (specifically in the MeV range) that mimics the terrestrial environment, as defined by the JEDEC standard JESD89 [53].

The spallation source ChipIr (UK) uses high-energy protons (700 MeV) on a tungsten target to generate a flux of $Y_n \sim 4.9 \times 10^6 \text{ n/cm}^2/\text{s}$ ($E_n > 10 \text{ MeV}$) [54], closely mimicking the atmospheric spectrum required by the standard. In the domain of compact accelerators, the proton-driven CANS at SHI-ATEX (Japan) utilizes a cyclotron with a low beam energy (18 MeV) and a beryllium target [55, 56]. Conversely, the electron-driven CANS in HUNS (Japan) employs a 32 MeV LINAC on a lead target, achieving a total neutron intensity of $\sim 5.0 \times 10^{12} \text{ n/s}$ [57]. This can be directly compared with the proposed SYNERGY source; utilizing a natural uranium target, the SYNERGY target reaches a fast rate of $1.2 \times 10^{15} \text{ n/s}$. This significantly higher neutron rate (nearly three orders of magnitude greater than HUNS) allows for a much higher acceleration rate, drastically reducing the time required for comprehensive soft error testing.

BNCT. BNCT has historically relied on neutron beams from research reactors, which enabled most early clinical trials but severely limited wider clinical deployment because only a few specialized reactors worldwide could provide suitable thermal or epithermal fluxes [58]. With the advent of Accelerator-Based Neutron Sources (ABNS), a technological shift is underway: cyclotrons, electrostatic tandem accelerators, and proton linacs now generate epithermal neutron beams that meet or exceed the IAEA-recommended flux intensity of $10^9 \text{ n/cm}^2/\text{s}$ and beam-quality constraints for clinical BNCT [36, 59]. Clinical or near-clinical proton-accelerator systems include the cyclotron-based C-BENS and hospital systems in Japan and Finland, as well as linac- and tandem-based sources using Li or Be targets that have demonstrated compliant epithermal fluxes in the required 0.5 eV–10 keV range [60]. In contrast, electron linac-based neutron concepts for BNCT remain at the feasibility or prototype stage: designs using high-energy electrons to generate neutrons in targets show that compact neutron sources are possible, but beam parameters and beam shaping assemblies still face substantial challenges in delivering continuous, hospital-scale epithermal fluxes comparable to proton systems and to IAEA recommendations [61]. More broadly, recent reviews emphasize that ABNS development has focused almost exclusively on low-to mid-energy proton or deuteron drivers on Li, Be, C or Sc targets, while higher energy linacs or synchrotrons are only mentioned generically and without detailed beam-parameter studies or clinical beam designs [62]. Current ABNS research is dominated by proton-driven source, whereas electron-linacs are still mostly

Table 5: Comparison of representative facilities and achievable neutron or photon rates for key applications. SYNERGY values refer to the results obtained in this work from a single synchrotron beamline.

Application	Spallation	CANS-p	CANS-e	SYNERGY
ADS studies	MYRRHA (Belgium) pLINAC target: LBE $S_n \sim 2 \times 10^{17}$ n/s $P_{beam} = 2.4$ MW (600 MeV) [38, 39]	CPHS (China) pLINAC target: ^9Be $S_n \sim 1 \times 10^{13}$ n/s $P_{beam} = 16$ kW (13 MeV) [40]	KIPT (Ukraine) eLINAC target: U $S_n \sim 3.0 \times 10^{14}$ n/s $P_{beam} = 100$ kW (100 MeV) [12, 13]	$S_n \sim 1.3 \times 10^{15}$ n/s target: U_{nat}
Soft-error testing	ChipIr (UK) p-synchrotron target: W $\phi_n \sim 4.9 \times 10^6$ n/cm ² /s ($E_n > 10$ MeV) $P_{beam} = 28$ kW (700 MeV) [54]	SHI-ATEX (Japan) cyclotron target: Be $\phi_n \sim 2 \times 10^5$ n/cm ² /s (thermal) $P_{beam} = 0.36$ kW (18 MeV) [55, 56]	HUNS (Japan) eLINAC target: Pb $S_n \sim 5.0 \times 10^{12}$ n/s (fast) $P_{beam} = 3.2$ kW (32 MeV) [57]	$S_n \sim 1.2 \times 10^{15}$ n/s target: U_{nat} (fast)
Application	Reactors	CANS-p	CANS-e	SYNERGY
Isotope production $(n, \gamma), (n, p)$	BR-2 (Belgium) $\phi_n \sim 10^{15}$ n/cm ² /s [64]	CPHS (China) pLINAC target: ^9Be $S_n \sim 1 \times 10^{13}$ n/s $P_{beam} = 16$ kW (13 MeV) [40]	EBC (India) eLINAC target: Ta $\phi_n \sim 10^7$ n/cm ² /s $P_{beam} = 1\text{-}3$ MW (10 MeV) [65]	$S_n \sim 1.3 \times 10^{15}$ n/s target: U_{nat}
Isotope production $(\gamma, n), (\gamma, p)$	–	–	Lighthouse (Germany) eLINAC target: None ϕ_γ not specified $P_{beam} = 130$ kW (75 MeV) [41]	$S_\gamma = 2.02 \times 10^{17}$ γ /s No target
BNCT	THOR (Taiwan) $\phi_n \sim 1.7 \times 10^9$ n/cm ² /s [66]	NUANS (Japan) Dynamitron target: Li $\phi_n \sim 10^9$ n/cm ² /s $P_{beam} = 42$ kW (1.9-2.8 MeV) [6]	PNS Project (Iran) eLINAC target: W $\phi_n \sim 5 \times 10^7$ n/cm ² /s $P_{beam} = 460$ kW (20 MeV) [67]	$S_n \sim 2.3 \times 10^{14}$ n/s target: ^9Be (epithermal)

limited to conceptual or early experimental studies. In addition, synchrotron-based BNCT source designs are largely absent from the existing literature. This clearly indicates a research gap in the systematic evaluation of synchrotron beams as drivers for epithermal neutron sources suitable for BNCT [63].

Within this context, the results presented in this paper provide a first quantitative indication of the potential of synchrotron-driven neutron sources for BNCT applications. By utilizing, for instance, a pure beryllium target, which not only generates neutrons efficiently but also naturally moderates the spectrum toward the epithermal energy range required for therapy, the source is shown to achieve a neutron rate of 2.7×10^{14} n/s. While a full clinical assessment of beam quality, dose distribution, and beam-shaping assemblies lies outside the scope of the present work, these results are nonetheless promising in demonstrating the feasibility of employing synchrotron-driven photonuclear neutron sources as BNCT drivers. A dedicated study, currently under development, will address the viability of the SYNERGY concept for BNCT.

5. Conclusions

In this work, the SYNERGY concept has been introduced and quantitatively assessed as a novel class of synchrotron-driven photoneutron source. By exploiting high-energy synchrotron radiation as an external photon driver, the proposed system fundamentally decouples the electron deceleration that leads to photon generation from the neutron production, overcoming the thermal and power-density limitations that constrain conventional proton and electron-linac-based compact neutron sources. This architectural separation enables the delivery of photon beam powers on the order of 200 kW per beamline while maintaining manageable target heating and peak energy deposition.

As a first analysis of this concept, a comprehensive parametric study has been conducted to optimize the geometry and evaluate the performance of several candidate target materials, spanning both low- Z moderating converters and high- Z neutron-producing materials. Monte Carlo simulations performed with OpenMC, MCNPX, and FLUKA show consistent trends in neutron yield and spectral shape, with discrepancies remaining within acceptable bounds given differences in nuclear data handling and physics models. The use of ENDF/B-VII.1 photonuclear data, known to provide conservative estimates, implies that the reported neutron yields should be interpreted as lower bounds of the achievable performance.

The results demonstrate that synchrotron-driven photoneutron sources can deliver, from each beamline, neutron source rates ranging from $\sim 3 \times 10^{14}$ n/s for moderating targets to more than 1×10^{15} n/s for uranium-based converters, with spectra naturally tailored to different application domains. When extended to a full synchrotron configuration comprising 50 beamlines, the corresponding total neutron intensity spans from approximately 1.5×10^{16} to beyond 5×10^{16} n/s. Within this framework, fast neutron fields compatible with accelerator-driven subcritical system studies, high-intensity environments for accelerated soft-error testing, and intrinsically moderated spectra relevant to BNCT and neutron scattering can all be achieved through appropriate target selection.

Beyond absolute performance, the inherent multi-beamline capability of large synchrotrons constitutes a distinctive advantage of the SYNERGY concept. It enables the simultaneous operation of multiple independent neutron stations, each optimized for different applications within a single facility, thereby substantially enhancing both the scientific reach and the cost-effectiveness of the infrastructure compared with conventional single-beam accelerator-driven sources.

Overall, this first feasibility assessment establishes synchrotron-driven photoneutron production as a credible and competitive alternative in the medium to high-flux neutron regime. Future work will address detailed thermal–mechanical target design, shielding, and application-specific systems, with particular emphasis on subcritical reactor coupling and medical neutron beam shaping.

Funding

This research did not receive any specific grant from funding agencies in the public, commercial, or not-for-profit sectors.

Acknowledgements

The authors would like to acknowledge Professor Enrico Padovani for granting access to the MCNPX code. They also wish to thank Guy Stein for developing the OpenMC photonuclear physics branch and for his valuable support throughout the analysis.

Data Availability Statement

The data that support the findings of this study are available from the corresponding author upon reasonable request.

Author Contribution Statement

A.C., L.L., and A.M. conceived the project. L.L. performed the parametric optimization and primary Monte Carlo simulations with assistance from A.M. A.M. conducted the multi-code validation and independent transport simulations using the FLUKA code. D.A. and H.H.B. defined the accelerator physics parameters, including the 32 GeV storage ring configuration and the 15 T dipole magnet characteristics. L.L. handled the spectral data analysis and figure preparation. L.L. wrote the manuscript, while A.M. revised it with input from all authors. A.C. supervised the study.

List of Symbols

Acronyms

ADS	Accelerator Driven System
BNCT	Boron Neutron Capture Therapy
CANS	Compact Accelerator-driven Neutron Source
CANS-p	Proton-driven Compact Accelerator-driven Neutron Source
CANS-e	Electron-driven Compact Accelerator-driven Neutron Source
GDR	Giant Dipole Resonance
LINAC	Linear Accelerator
PEDD	Peak Energy Deposition Density
RF	Radio Frequency
SEE	Single Event Effects
SYNERGY	Synchrotron-driven NEutron source for Research, enerGY and therapY

Greek Symbols

γ	Photon (gamma radiation)
σ	Microscopic cross section
σ_{tot}	Total microscopic photon interaction cross section
$\sigma_{\gamma,n}$	Photonuclear single-neutron emission cross section

$\sigma_{\gamma,2n}$	Photonuclear double-neutron emission cross section
$\sigma_{\gamma,f}$	Photonuclear fission cross section
$\nu_{\gamma,f}$	Average number of neutrons emitted per photofission
ϕ_n	Neutron flux

Latin Symbols

B	Magnetic field strength at photon source point
Y_n	Photoneutron yield (neutrons per source photon)
S_n	Photoneutron source rate (neutrons per second)
S_γ	Incident photon source strength
N_γ	Number of simulated source photons
E_γ	Photon energy
E_e	Electron energy
R	Target radius
L	Target length
P	Beam or photon power
A	Mass number
Z	Atomic number

References

- [1] Bauer, G. S. Neutron sources. Tech. Rep. OSTI ID 20009243, Paul Scherrer Institut (PSI), Villigen, Switzerland (2001). URL <https://www.osti.gov/etdeweb/servlets/purl/20009243>. Available via OSTI/ETDE.
- [2] Rush, J. J. US neutron facility development in the last half-century: A cautionary tale. *Physics in Perspective* **17**, 135–155 (2015).
- [3] Knoll, G. F. *Radiation Detection and Measurement* (John Wiley & Sons, New York, 2010), 4th edn. See Chapter 1: Radiation Sources.
- [4] Kiyanagi, Y. Neutron applications developing at compact accelerator-driven neutron sources. *AAPPS Bulletin* **31** (2021).
- [5] Carpenter, J. M. The development of compact neutron sources. *Nature Reviews Physics* **1**, 177–179 (2019).
- [6] Anderson, I., Andreani, C., Carpenter, J. *et al.* Research opportunities with compact accelerator-driven neutron sources. *Physics Reports* **654**, 1–58 (2016).
- [7] Gutberlet, T. *et al.* High current accelerator-driven neutron sources - the hbs project for a next generation neutron facility. *Nuclear Science and Technology Open Research* **3**, 10 (2025).

- [8] Lai, Y. & Yang, Y. A design for the high yield photoneutron source target station. *Materials* **15** (2022).
- [9] Ridikas, D., Safa, H. & Giacri, M. Conceptual study of neutron irradiation-driven by electron accelerator. In *7th Information Exchange Meeting - Jeju (Republic of Korea)* (2002).
- [10] Findlay, D. Applications of photonuclear reactions. *Nuclear Instruments & Methods in Physics Research Section B-beam Interactions With Materials and Atoms* (1990).
- [11] Herrador, J. O. *et al.* Performance of high-intensity electron linacs as drivers for compact neutron sources (2025).
- [12] Gohar, Y., Bolshinsky, I. & Karnaukhov, I. Neutron source facility of the national science center "kharkiv institute of physics and technology" at kharkiv, ukraine. Tech. Rep. ANL/NE-21/4, Argonne National Lab. (ANL), Argonne, IL (United States) (2021). URL <https://www.osti.gov/biblio/1900255>. Accessed via OSTI.gov.
- [13] Mytsykov, A. *et al.* The Progress in Physical Start-Up of the NSC KIPT Subcritical Neutron Source Facility Driven by an Electron Linear Accelerator. In *Proc. 10th International Particle Accelerator Conference (IPAC'19), Melbourne, Australia, 19-24 May 2019*, no. 10 in International Particle Accelerator Conference, 2197–2199 (JACoW Publishing, Geneva, Switzerland, 2019).
- [14] Loi, L., Missaglia, A., Alesini, D., Braun, H. H. & Cammi, A. Optimization of synchrotron-based photoneutron sources for subcritical systems. In *PHYSOR 2026 - The International Conference on Physics of Reactors*, pp (Torino, Italy, 2026).
- [15] Kamitsubo, H. SPring-8 Program. *Journal of Synchrotron Radiation* **5**, 162–167 (1998).
- [16] Gryaznykh, D., Lykov, V. & Plokhoi, V. Estimations of neutron yield from beryllium target irradiated by spring-8 hard synchrotron radiation. *Nuclear Instruments and Methods in Physics Research Section A: Accelerators, Spectrometers, Detectors and Associated Equipment* **448**, 106–108 (2000).
- [17] Asano, Y. & Kawashima, Y. Calculations for the availability of photoneutron using synchrotron radiation. *Radiation Protection Dosimetry* **115**, 176–180 (2005).
- [18] Alesini, D. Perspectives of transmutation, controlled fission and characterization of materials with high-intensity electron accelerators. https://agenda.infn.it/event/39081/contributions/218867/attachments/116508/167944/2024-02-22_Alesini.pdf (2024). Presented at Workshop Transizione Energetica INFN-E INFN-A.
- [19] Tanaka, T. & Kitamura, H. *SPECTRA*: a synchrotron radiation calculation code. *Journal of Synchrotron Radiation* **8**, 1221–1228 (2001).
- [20] Chao, A. W., Tigner, M., Weise, H. & Zimmermann, F. *Handbook of accelerator physics and engineering* (World scientific, 2023).

[21] Willeke, F. *The HERA lepton–proton collider*, chap. Chapter 15, 225–242 (World Scientific, 2021).

[22] Fynan, D. A., Seo, Y., Kim, G., Barros, S. & Kim, M. J. Photoneutron production in heavy water reactor fuel lattice from accelerator-driven bremsstrahlung. *Annals of Nuclear Energy* **155**, 108141 (2021).

[23] Balabanski, D. L. & Constantin, P. 80 years of experimental photo-fission research. *Eur. Phys. J. A* **60**, 39 (2024).

[24] Caldwell, J., Dowdy, E., Alvarez, R., Berman, B. & Meyer, P. Experimental determination of photofission neutron multiplicities for ^{235}U , ^{236}U , ^{238}U , and ^{232}Th using monoenergetic photons. *Nuclear Science and Engineering* **73**, 153–163 (1980).

[25] Filipescu, D. *et al.* Giant dipole resonance photofission and photoneutron reactions in ^{238}U and ^{232}Th . *Phys. Rev. C* **109**, 044602 (2024).

[26] Sari, A. Characterization of photoneutron fluxes emitted by electron accelerators in the 4–20mev range using monte carlo codes: A critical review. *Applied Radiation and Isotopes* **191**, 110506 (2023).

[27] Sari, A. *et al.* A benchmark for monte carlo simulation of photoneutron fields from electron accelerators. *Nuclear Instruments and Methods in Physics Research Section A: Accelerators, Spectrometers, Detectors and Associated Equipment* **1072**, 170168 (2025).

[28] Garnaud, Louis *et al.* Compendium on monte carlo simulation of photoneutrons in the giant dipole resonance energy range: The first five elements. *EPJ Web Conf.* **302**, 07004 (2024).

[29] Kawano, T. *et al.* IAEA photonuclear data library 2019. *Nuclear Data Sheets* **163**, 109–162 (2020).

[30] Iwamoto, O. *et al.* Japanese evaluated nuclear data library version 5: JENDL-5. *Journal of Nuclear Science and Technology* **60**, 1–60 (2023).

[31] Chadwick, M., Obložinský, P. *et al.* ENDF/B-VII.0: Next generation evaluated nuclear data library for nuclear science and technology. *Nuclear Data Sheets* **107**, 2931–3118 (2006). URL <https://www.sciencedirect.com/science/journal/00903752>.

[32] Stein, G. Openmc with photonuclear physics. <https://github.com/GuySten/openmc/tree/photonuclear-physics> (2024). Accessed: October 2025.

[33] Loi, L. *et al.* Verification of photonuclear reactions in openmc with mcnpnx and fluka. In *PHYSOR 2026 - The International Conference on Physics of Reactors*, pp (Torino, Italy, 2026).

[34] Pelowitz, D. B. *et al.* MCNPXTM User’s Manual, Version 2.7.0. Tech. Rep. LA-CP-11-00438, Los Alamos National Laboratory, Los Alamos, NM, USA (2011).

[35] Battistoni, G. *et al.* Overview of the fluka code. *Annals of Nuclear Energy* **82**, 10–18 (2015). Joint International Conference on Supercomputing in Nuclear Applications and Monte Carlo 2013, SNA + MC 2013. Pluri- and Trans-disciplinarity, Towards New Modeling and Numerical Simulation Paradigms.

[36] Ahmed, M. *et al.* *Advances in Boron Neutron Capture Therapy*. No. 18 in Human Health Reports (International Atomic Energy Agency, Vienna, 2023).

[37] Bowman, C. *et al.* Nuclear energy generation and waste transmutation using an accelerator-driven intense thermal neutron source. *Nuclear Instruments & Methods in Physics Research Section A-accelerators Spectrometers Detectors and Associated Equipment* (1992).

[38] Abderrahim, H. A. *et al.* Myrrha, a multipurpose hybrid research reactor for high-end applications. *Nuclear Physics News* (2010).

[39] De Bruyn, D. Development of Advanced Reactor Systems: The MYRRHA Project. Presentation at the SNETP Forum 2021 (TS1: SMRs and AMR 1) (2021). URL https://snetp.eu/wp-content/uploads/2021/02/Presentation_Didier-De-Bruyn.pdf. Last access: January 2026.

[40] Wang, X., Xing, Q., Loong, C.-K., Guan, X. & Du, T. Delivery of 3-mev proton and neutron beams at cphs: A status report on accelerator and neutron activities at tsinghua university. *Physics Procedia* **60**, 186–192 (2014). 3rd International Meeting of the Union for Compact Accelerator-driven Neutron Sources, UCANS III, 31 July–3 August 2012, Bilbao, Spain & the 4th International Meeting of the Union for Compact Accelerator-driven Neutron Sources, UCANS IV, 23–27 September 2013, Sapporo, Hokkaido, Japan.

[41] Kramer, K. *et al.* Lighthouse: A Superconducting Electron Linac for Commercial Production of Medical Radioisotopes. In *Proc. 13th Int. Particle Accelerator Conf. (IPAC'22)*, 2537–2539 (JACoW Publishing, Bangkok, Thailand, 2022).

[42] Schubert, H., Leonte, R., Băruță, S., Negoita, F. & Niculae, D. Production of medical radioisotopes via photonuclear reactions: review of candidates and opportunities for the planned radioactive ion facility at ifin-hh. *Romanian Reports in Physics* **76**, 203–203 (2024).

[43] International Atomic Energy Agency. Photonuclear production of radioisotopes. Tech. Rep. 2051, International Atomic Energy Agency, Vienna (2024). URL <https://www-pub.iaea.org/MTCD/publications/PDF/TE-2051web.pdf>.

[44] Van der Marck, S. C., Koning, A. J. & Charlton, K. The options for the future production of the medical isotope ^{99}mo . *European Journal of Nuclear Medicine and Molecular Imaging* **37**, 1817–1820 (2010).

[45] Konefał, A., Orlef, A. & Sokół, M. Application of therapeutic linear accelerators for the production of radioisotopes used in nuclear medicine. *Polish Journal of Medical Physics and Engineering* **28**, 107–116 (2022).

[46] Wang, Y. *et al.* Production review of accelerator-based medical isotopes. *Molecules* **27** (2022).

[47] Capogni, M. *et al.* 14 mev neutrons for $^{99}\text{mo}/^{99m}\text{tc}$ production: experiments, simulations and perspectives. *Molecules* **23** (2018).

[48] Pang, X. *et al.* Progress of photonuclear cross sections for medical radioisotope production at the slegs energy domain. *Nuclear Science and Techniques* **34** (2023).

[49] Kazakov, A., Ekatova, T. & Babenya, J. Photonuclear production of medical radiometals: a review of experimental studies. *Journal of Radioanalytical and Nuclear Chemistry* **328**, 493–505 (2021).

[50] Habs, D. & Köster, U. Production of medical radioisotopes with high specific activity in photonuclear reactions with γ -beams of high intensity and large brilliance. *Applied Physics B* **103**, 501–519 (2010).

[51] Budker, D. *et al.* Expanding nuclear physics horizons with the gamma factory. *Annalen der Physik* **534** (2021).

[52] Ju, K., Lee, J., Rehman, H. & Kim, Y. A feasibility study on photo-production of ^{99m}tc with the nuclear resonance fluorescence. *Nuclear Engineering and Technology* (2019).

[53] JEDEC Solid State Technology Association, Arlington, VA. *Measurement and Reporting of Alpha Particle and Terrestrial Cosmic Ray-Induced Soft Errors in Semiconductor Devices* (2006). JEDEC Standard JESD89A.

[54] Cazzaniga, C. & Frost, C. D. Progress of the scientific commissioning of a fast neutron beamline for chip irradiation. *Journal of Physics: Conference Series* **1021**, 012037 (2018).

[55] Kiyanagi, Y. Neutron imaging at compact accelerator-driven neutron sources in japan. *Journal of Imaging* **4** (2018).

[56] Kiyanagi, Y. Compact accelerator-driven neutron sources (canss) and their applications in japan. Presentation at SPES Workshop, Ferrara, Italy (2019). URL https://agenda.infn.it/event/16937/contributions/34806/attachments/60751/72137/SPES-CANS20190130_KYANAGI.pdf.

[57] Sato, H. *et al.* 50th anniversary and recent decade achievements of the hokkaido university neutron source (huns) facility with cold-fast neutrons and high-energy electrons/x-rays. *EPJ Web of Conferences* **298**, 05006 (2024).

[58] Jin, W. H., Seldon, C., Butkus, M., Sauerwein, W. & Giap, H. A review of boron neutron capture therapy: Its history and current challenges. *International Journal of Particle Therapy* **9**, 71 – 82 (2022).

[59] Bae, Y. *et al.* Advances of linac-based boron neutron capture therapy in korea. *AAPPS Bulletin* **32**, 1–23 (2022).

- [60] Miyatake, S., Wanibuchi, M., Hu, N. & Ono, K. Boron neutron capture therapy for malignant brain tumors. *Journal of Neuro-Oncology* **149**, 1 – 11 (2020).
- [61] Kasilov, V. *et al.* Concept of neutron source creation for nuclear medicine on the basis of linear electron accelerator. *4* (2021).
- [62] Verdera, A. & Praena, J. Study on novel neutron irradiation without beam shaping assembly in boron neutron capture therapy. *Scientific Reports* **14** (2024).
- [63] Dymova, M. A., Taskaev, S. Y., Richter, V. & Kuligina, E. Boron neutron capture therapy: Current status and future perspectives. *Cancer Communications* **40**, 406 – 421 (2020).
- [64] Hasan, S. & Prelas, M. A. Molybdenum-99 production pathways and the sorbents for $^{99}\text{Mo}/^{99m}\text{Tc}$ generator systems using (n, γ) ^{99}Mo : a review. *SN Applied Sciences* **2**, 1782 (2020).
- [65] Deo, K. *et al.* Measurement of effective $^{98}\text{Mo}(\text{n}, \gamma)$ 99 mo reaction cross-section in the epi-cadmium neutron flux produced by 10 mev electron linac with ta-beo assembly. *Journal of Radioanalytical and Nuclear Chemistry* **333**, 3793 – 3806 (2024).
- [66] Tung, C., Wang, Y., Hsu, F., Chang, S. & Liu, Y.-W. Characteristics of the new thor epithermal neutron beam for bnct. *Applied Radiation and Isotopes* **61**, 861–864 (2004). Topics in Neutron Capture Therapy: Proceedings of the Eleventh World Congress on Neutron Capture Therapy (ISNCT-11).
- [67] Pazirandeh, A., Torkamani, A. & Taheri, A. Design and simulation of a neutron source based on an electron linear accelerator for bnct of skin melanoma. *Applied Radiation and Isotopes* **69**, 749–755 (2011).